

DECIPHERING THE ATMOSPHERIC COMPOSITION OF WASP-12b:
A COMPREHENSIVE ANALYSIS OF ITS DAYSIDE EMISSION

KEVIN B. STEVENSON¹, JACOB L. BEAN¹, NIKKU MADHUSUDHAN^{2,3}, AND JOSEPH HARRINGTON⁴

¹Department of Astronomy and Astrophysics, University of Chicago, 5640 S Ellis Ave, Chicago, IL 60637, USA

²Institute of Astronomy, University of Cambridge, Madingley Road, Cambridge, CB3 0HA, UK

³Department of Physics & Department of Astronomy, Yale University, P.O. Box 208120, New Haven, CT 06520, USA and

⁴Planetary Sciences Group, Department of Physics, University of Central Florida, Orlando, FL 32816-2385, USA

ABSTRACT

WASP-12b was the first planet reported to have a carbon-to-oxygen ratio (C/O) greater than one in its day-side atmosphere. However, recent work to further characterize its atmosphere and confirm its composition has led to incompatible measurements and divergent conclusions. Additionally, the recent discovery of stellar binary companions $\sim 1''$ from WASP-12 further complicates the analyses and subsequent interpretations. We present a uniform analysis of all available *Hubble* and *Spitzer Space Telescope* secondary-eclipse data, including previously-unpublished *Spitzer* measurements at 3.6 and 4.5 μm . The primary controversy in the literature has centered on the value and interpretation of the eclipse depth at 4.5 μm . Our new measurements and analyses confirm the shallow eclipse depth in this channel, as first reported by Campo and collaborators and used by Madhusudhan and collaborators to infer a carbon-rich composition. To explain WASP-12b's observed dayside emission spectrum, we implemented several recent retrieval approaches. We find that when we exclude absorption due to C_2H_2 and HCN, which are not universally considered in the literature, our models require implausibly large atmospheric CO_2 abundances, regardless of the C/O. By including C_2H_2 and HCN in our models, we find that a physically-plausible carbon-rich solution achieves the best fit to the available photometric and spectroscopic data. In comparison, the best-fit oxygen-rich models have abundances that are inconsistent with the chemical equilibrium expectations for hydrogen-dominated atmospheres and are 670 times less probable. Our best-fit solution is also 7.3×10^6 times more probable than an isothermal blackbody model.

Subject headings: planetary systems — stars: individual: WASP-12 — techniques: photometric, spectroscopic

1. INTRODUCTION

The study of exoplanetary atmospheres has shown that planets are a diverse group of objects and that placing constraints on their composition and chemistry will advance our understanding of planet formation and planetary physics. Detailed characterization of hot Jupiters is possible when these planets pass in front of or behind their parent stars. The latter event, known as the secondary eclipse, reveals a planet's dayside emission spectrum using measurements at multiple infrared wavelengths. By comparing atmospheric models to the measured spectrum, we can place constraints on the absolute chemical abundances and thermal profile.

At the time of its discovery, WASP-12b was the most heavily-irradiated exoplanet yet known, with an equilibrium temperature in excess of 2500 K (Hebb et al. 2009). This afforded an excellent opportunity to measure the planet's dayside thermal emission over a broad range of infrared wavelengths. These data were used to place constraints on the planet's atmospheric composition and thermal profile; however, independent interpretations of the individual data sets have led to different conclusions. Therefore, we conducted a uniform analysis of all available *Hubble* and *Spitzer Space Telescope* secondary eclipse data, including previously-unpublished *Spitzer* measurements at 3.6 and 4.5 μm , to assemble a more consistent description of the planet's atmospheric composition and thermal profile.

In a previous report, we used *Spitzer* to measure the dayside emission of WASP-12b at four infrared wave-

lengths (Campo et al. 2011). We combined these data with secondary-eclipse depths measured in the J, H, and Ks bands (Croll et al. 2011) and found that the best-fit atmospheric models favored a carbon-to-oxygen ratio (C/O) ≥ 1 (Madhusudhan et al. 2011). For comparison, the solar C/O is ~ 0.54 .

Due to WASP-12b's small semi-major axis and inflated radius, the planet's shape may not be spherical, but that of a prolate spheroid instead. Using full-orbit observations of WASP-12b with *Spitzer*, Cowan et al. (2012) measured significant ellipsoidal variations at 4.5 μm , but no variations at 3.6 μm . Under this scenario, they reported eclipse depths that are consistent with previous results. However, by fixing the ellipsoidal variations to zero (the null hypothesis), Cowan et al. (2012) noted that the measured eclipse depths favor a solar C/O and a modest thermal inversion. To make this determination, they varied the abundance of CO as a proxy for varying the C/O in their 1D radiative transfer models.

Further obfuscating the planet's atmospheric composition, Bergfors et al. (2013) announced the discovery of a companion star only $1''$ (less than one *Spitzer* pixel) from WASP-12. Bechter et al. (2014) and Sing et al. (2013) have since demonstrated that the companion is a binary (labeled WASP-12BC) that is physically associated with the primary star WASP-12A. Upon determining that the companions are of stellar type M0 – M1, Crossfield et al. (2012) combined results from a narrow-band, 2.315- μm secondary-eclipse measurement with a corrected, weighted average of previously-reported eclipse depths, assuming the null hypothesis from Cowan et al. (2012). Following Barman et al. (2001, 2005),

they also constructed a variety of atmospheric models for comparison. Using χ^2 and Bayesian Information Criterion (BIC) values as their metrics, they concluded that a black-body approximates WASP-12b’s emission spectrum well, and that its photosphere is nearly isothermal.

Both López-Morales *et al.* (2010) and Föhring *et al.* (2013) observed WASP-12b in the z' band (centered at 0.9 μm) during secondary eclipse; however, their reported depths ($0.082 \pm 0.015\%$ and $0.130 \pm 0.013\%$, respectively) are discrepant by $> 3\sigma$. This difference may be the result of temporal variability in the planet flux or unmodeled systematics in one or both analyses.

Using observations from the Wide-Field Camera 3 (WFC3) instrument on board the *Hubble Space Telescope* (HST) and two different atmospheric modeling approaches (optimal estimation and Markov-chain Monte Carlo (MCMC) retrieval), Swain *et al.* (2013) found that the companion-stars-corrected dayside spectrum is best fit by an H_2 atmosphere with no additional opacity sources. Such a model supports the isothermal findings of Crossfield *et al.* (2012). When including the standard opacity sources (H_2O , CH_4 , CO , and CO_2), Swain *et al.* (2013) found no evidence for a $\text{C/O} \geq 1$ or a thermal inversion.

Using the published results from Crossfield *et al.* (2012) and Swain *et al.* (2013), Line *et al.* (2014) carried out a temperature and abundance retrieval analysis of eight exoplanets, including WASP-12b. They used a suite of inverse modeling algorithms, called CHIMERA, which employ multiple Bayesian retrieval approaches and found two possible atmospheric scenarios. Their preferred mode (“null”) favors a weak thermal inversion and a large CO_2 abundance. A secondary mode (“ellipsoidal”) results in a slightly stronger thermal inversion and an even higher CO_2 mixing ratio. Both scenarios favor a solar C/O , but larger ratios closer to unity cannot be ruled out.

In this paper, we present new broadband secondary-eclipse observations of WASP-12b at 3.6 and 4.5 μm using *Spitzer*. We combine these data with reanalyses of previously published *Spitzer* InfraRed Array Camera (IRAC, Fazio *et al.* 2004) eclipse observations (Campo *et al.* 2011; Cowan *et al.* 2012) and emission-spectroscopy observations using *HST*/WFC3 (Swain *et al.* 2013). We also account for the contamination by WASP-12BC. The work presented here tests a variety of modeling approaches, including that of Line *et al.* (2014), and offers a comprehensive and uniform analysis of available WASP-12b secondary-eclipse data to constrain its dayside atmospheric composition.

2. SPITZER/IRAC OBSERVATIONS AND DATA ANALYSIS

2.1. Observations and Reduction

For the new observations presented here, *Spitzer*’s IRAC acquired 2109 frames of WASP-12 in each of the 3.6 and 4.5 μm channels (Program 60003, PI Joseph Harrington). As with the observations presented by Campo *et al.* (2011), we used 12-second exposures in full-frame mode and achieved a duty cycle of almost 80%. Conversely, the observations presented by Cowan *et al.* (2012, Program 70060, PI Pavel Machalek) used 0.4-second exposures in subarray mode and, due to a 104-second gap between subarray sets, have a duty cycle of $\sim 18\%$. Therefore, the latter achieved approximately half of the precision obtained with the full-array observations. Additional observation information is listed in Table 1.

We produce systematics-corrected light curves using the Photometry for Orbits, Eclipses, and Transits (POET) pipeline (Campo *et al.* 2011; Stevenson *et al.* 2012; Cubillos *et al.* 2013). POET flags bad pixels using a two-iteration, 4σ filter along the time axis of each set of 64 frames, calculates image centers from a 2D Gaussian fit, and applies $5\times$ interpolated aperture photometry (Harrington *et al.* 2007) for apertures up to 5.0 pixels in radius. It then removes systematics and fits lightcurve models as described below.

2.2. Light-Curve Systematics and Fits

Spitzer light curves exhibit several well characterized systematics (Charbonneau *et al.* 2005; Agol *et al.* 2010; Knutson *et al.* 2011; Stevenson *et al.* 2012; Lewis *et al.* 2013). We test polynomial and exponential functions when modeling the time-dependent systematics at all wavelengths and apply Bilinearly-Interpolated Subpixel Sensitivity (BLISS) mapping (Stevenson *et al.* 2012) to model the position-dependent systematics at 3.6 and 4.5 μm , except for wa012bs21, which does not exhibit this effect. This is unusual for this array, but has been seen occasionally (e.g., Todorov *et al.* 2010).

Simultaneously with the systematics, we fit the secondary eclipses with the uniform-source equations from Mandel & Agol (2002). We perform a joint, simultaneous fit of the 3.6 and 5.8 μm observations as well as a separate joint fit for the 4.5 and 8.0 μm observations. For the 2008 observations, IRAC observed these channel pairs simultaneously, so the fits share the eclipse midpoint. In each joint fit, the light curves at the same wavelength share one eclipse depth. We estimate uncertainties using two techniques, differential-evolution MCMC (DE-MCMC) and residual permutation. The latter produces slightly larger uncertainties, which we adopt. Using the transit parameters from Stevenson *et al.* (2014), we fix the eclipse duration (0.11459 orbits) and ingress/egress times (0.01557 orbits). Allowing these parameters to vary does not change our final results. Figure 1 displays binned, systematics-corrected light curves with best-fit models.

Individual analyses of the *Spitzer* eclipses produced depths that are consistent with the joint fits to within 1σ at 3.6 μm and to within 2σ at 4.5 μm . See Table 2 for the individual eclipse depths using a 3.0 pixel aperture size. It is intriguing that both 4.5 μm eclipse depth measurements extracted from the phase curve observation are deeper than the remaining secondary eclipse measurements.

As with Cowan *et al.* (2012), we do not include the 3.6- μm secondary eclipse from 2010 November 17 in our final analysis. This is due to the presence of a strong feature (possibly due to stellar activity) during the latter half of the eclipse that alters the measured depth. In contrast to Cowan *et al.* (2012), we do not fit the entire phase curves when determining the eclipse depths. This is to ensure that unmodeled flux variations in the phase curves do not affect the measured depths and bypasses the question of ellipsoidal variation. As reported by Stevenson *et al.* (2014), when we do fit the full phase curves, our best-fit models confirm the large ellipsoidal variations in only the 4.5 μm channel. Our measured eclipse depths are in excellent agreement ($< 1\sigma$) with those favored by Cowan *et al.* (2012, ellipsoidal variation models) and are inconsistent with the null hypothesis (no ellipsoidal variation) 4.5 μm depth by 10σ .

TABLE 1
OBSERVATION INFORMATION

Label ^a	Observation Date	Duration [minutes]	Frame Time [seconds]	Total Frames	<i>Spitzer</i> Pipeline	Wavelength [μm]	Previous Publications ^b
wa012bs21	October 29, 2008	338	12	1560	S18.25.0	4.5	Ca11, M11
wa012bs41	October 29, 2008	338	12	1560	S18.25.0	8.0	Ca11, M11
wa012bs11	November 3, 2008	367	12	1697	S18.25.0	3.6	Ca11, M11
wa012bs31	November 3, 2008	367	12	1697	S18.25.0	5.8	Ca11, M11
wa012bs22	May 3, 2010	460	12	2109	S18.18.0	4.5	-
wa012bs12	May 4, 2010	460	12	2109	S18.18.0	3.6	-
wa012bs13	November 18, 2010	427	0.4	12728	S18.18.0	3.6	Co12
wa012bs23	December 11, 2010	673	0.4	20000	S18.18.0	4.5	Co12
wa012bs24	December 12, 2010	427	0.4	12728	S18.18.0	4.5	Co12

^awa012b designates the planet, *s* specifies secondary eclipse, and ## identifies the wavelength and observation number.

^bCa11 = Campo et al. (2011), M11 = Madhusudhan et al. (2011), and Co12 = Cowan et al. (2012).

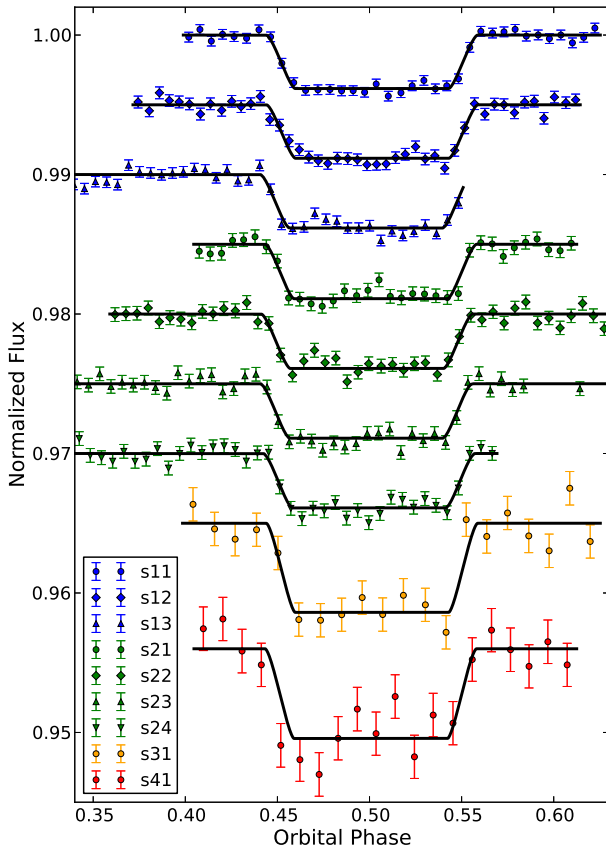


FIG. 1.— WASP-12b photometric light curves using *Spitzer*/IRAC. The results are corrected for systematics, normalized to the system flux, and shifted vertically for ease of comparison. The lines are best-fit models and the error bars are 1σ uncertainties. The shorthanded legend labels correspond to the last three characters in each event’s label (e.g., s11 = wa012bs11).

2.3. Dilution Factor Correction

A recently discovered, binary companion (Bergfors et al. 2013; Bechter et al. 2014) resides well within the *Spitzer* photometry apertures, thus diluting the measured eclipse depths. To correct for this effect, we apply the dilution factors calculated by Stevenson et al. (2014, $\alpha_{Comp}(3.6, 4.5, 5.8, 8.0) = 0.1149, 0.1196, 0.1207, 0.1190$) to each of the four *Spitzer* channels using the equation:

$$\delta_{Corr}(\lambda) = [1 + g(\beta, \lambda)\alpha_{Comp}(\lambda)] \delta_{Meas}(\lambda), \quad (1)$$

TABLE 2
INDIVIDUAL ECLIPSE DEPTHS USING A 3.0 PIXEL APERTURE SIZE

Label	Eclipse Depth [%]
wa012bs11	0.41 ± 0.02
wa012bs12	0.38 ± 0.02
wa012bs13	0.36 ± 0.02
wa012bs21	0.38 ± 0.02
wa012bs22	0.36 ± 0.02
wa012bs23	0.42 ± 0.02
wa012bs24	0.42 ± 0.02

where $\delta_{Meas}(\lambda)$ are the measured (or uncorrected) eclipse depths and $g(\beta, \lambda)$ are the wavelength-dependent companion flux fractions inside a photometric aperture of size β . Table 3 gives the final eclipse depths. Since we apply a single eclipse depth to fit all of the observations from a given channel, we select a single aperture size for each channel, thus allowing us to apply a single $g(\beta, \lambda)$ value during the correction. In our final analysis, we use an aperture size of 3.0 pixels for all channels. We tested aperture sizes up to a radius of 5.0 pixels in all channels and found no significant ($>1\sigma$) correlation with the measured eclipse depths. See Figure 2 for examples at 5.8 and 8.0 μm .

3. HST/WFC3 OBSERVATIONS AND DATA ANALYSIS

3.1. Observation and Reduction

Spanning five orbits on 2011 April 15, *HST* observed a secondary eclipse of WASP-12b using the WFC3 instrument with its G141 grism. Swain et al. (2013) provide additional details on the observations (Program 12230, PI Mark Swain). Using the reduction, extraction, and calibration steps described by Stevenson et al. (2014), we generate eleven wavelength-dependent light curves spanning 1.10 – 1.65 μm . See Berta et al. (2012), Deming et al. (2013), Sing et al. (2013), and Kreidberg et al. (2014) for additional discussion on WFC3 analyses and calibration.

3.2. Light-Curve Systematics and Fits

These data do not exhibit the strong persistence behavior between buffer dumps that is seen in some other WFC3 exoplanet light curves. We do, however, detect evidence for light-curve fluctuations due to thermal breathing of the telescope as it warms and cools while orbiting the Earth every ~ 96 minutes (see Figure 3). Previous analyses detect similar variations in the WFC3 WASP-12b transmission spectroscopy observations (Sing et al. 2013; Stevenson et al. 2014). To model the

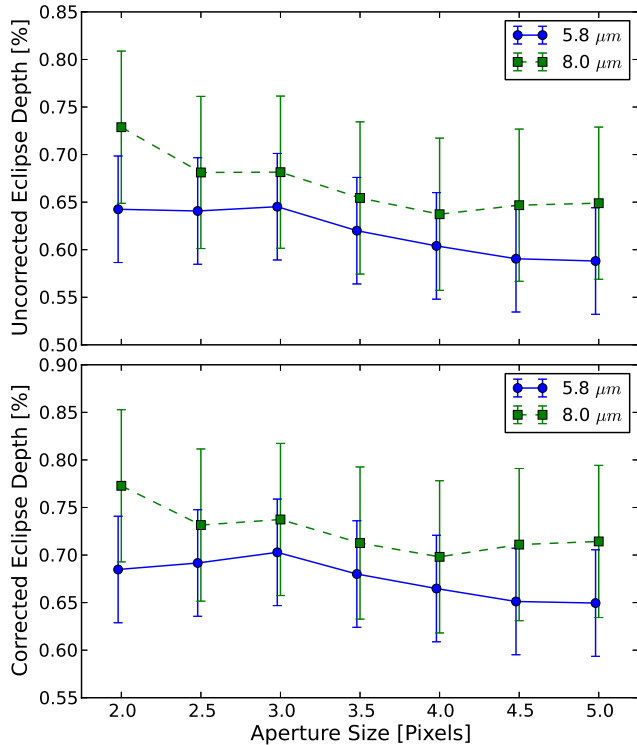


FIG. 2.— Measured (top) and companion-star corrected (bottom) eclipse depths at 5.8 and 8.0 μm . The measured eclipse depths may have a weak dependence on photometry aperture size; however, this trend is not significant as the points all fall within 1σ of each other. There is no discernible trend at 3.6 or 4.5 μm .

TABLE 3
COMPANION-STAR-CORRECTED ECLIPSE DEPTHS

Wavelength (μm)	RMS (ppm)	Eclipse Depth (%)
1.10 – 1.15	1512	0.119 ± 0.017
1.15 – 1.20	1374	0.128 ± 0.012
1.20 – 1.25	1263	0.101 ± 0.012
1.25 – 1.30	1203	0.142 ± 0.011
1.30 – 1.35	1274	0.154 ± 0.012
1.35 – 1.40	1242	0.156 ± 0.012
1.40 – 1.45	1296	0.184 ± 0.012
1.45 – 1.50	1299	0.198 ± 0.012
1.50 – 1.55	1407	0.196 ± 0.013
1.55 – 1.60	1563	0.179 ± 0.014
1.60 – 1.65	1760	0.192 ± 0.017
3.6	2296	0.421 ± 0.011
	2523	
	6326	
4.5	3214	0.428 ± 0.012
	3131	
	8182	
	8251	
5.8	10633	0.696 ± 0.060
8.0	13240	0.696 ± 0.096

white light curve, we use the uniform-source equations from Mandel & Agol (2002) for the secondary eclipse over orbits 2 – 5, a linear slope for the baseline, and a sinusoidal function for the thermal breathing.

To model the spectroscopic light curves, we apply both methods described by Stevenson *et al.* (2014). Method 1

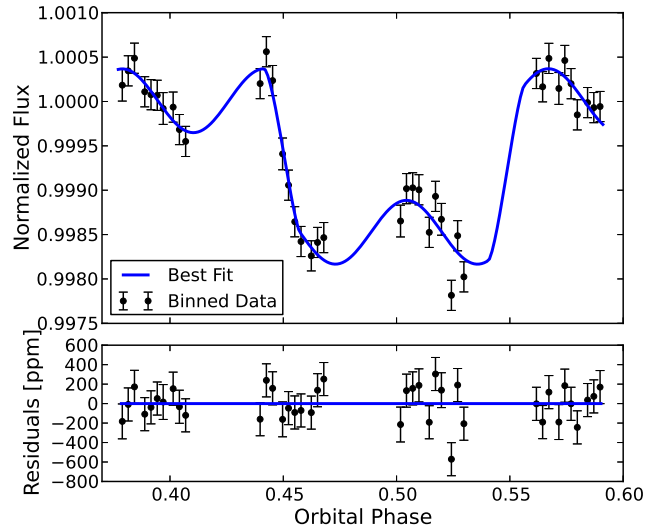


FIG. 3.— WASP-12b band-integrated light curve (top panel) with residuals (bottom panel) from 2011 April 15 using *HST*'s WFC3 instrument. The black data points are binned in phase and display 1σ uncertainties. The solid blue line depicts the best-fit model, which includes a sinusoidal function to model the effects of telescope thermal breathing.

uses the same functional form as the white light-curve analysis, with wavelength-independent systematic models and wavelength-dependent eclipse depths and baseline offsets. Method 2, also called *Divide-White*, fits all of the orbits using the white light curve to generate a non-analytic model of the wavelength-independent systematics. The only free parameters with this model are the wavelength-dependent secondary eclipse depths and baseline offsets. We estimate uncertainties with our DE-MCMC algorithm. In agreement with Swain *et al.* (2013), correlation plots of RMS vs. bin size indicate that there is no significant time-correlated noise in the data and, as such, there is no need to inflate uncertainty estimates (Pont *et al.* 2006; Winn *et al.* 2008). The WFC3 dataset has an insufficient number of points for a residual-permutation analysis. We plot the normalized spectroscopic light curves from Method 2 in Figure 4. The residual RMS values range from 1190 to 1640 ppm and the uncertainties range from 1.07 to $1.28\times$ the photon limit, with an average of $1.15\times$.

3.3. Dilution Factor Correction

The spectroscopic extraction technique employed above does not separate the WASP-12 signal from that of the companion stars. Therefore, we estimated the corrected eclipse depths in Table 3 using Equation 1 (where $g(\beta, \lambda) = 1$) and the companion star dilution factors given in Table 4 of Stevenson *et al.* (2014). Figure 5 displays the corrected eclipse depths from both techniques and compares the results to those from Swain *et al.* (2013). All but one of the spectroscopic channels agree to within 1σ . The source of the outlier is unknown. We apply Method 2 for the remainder of our analysis.

4. ATMOSPHERIC MODELS AND DISCUSSION

When deriving the best-fit atmospheric models, we use the eleven spectroscopic and four photometric eclipse depths listed in Table 3. Additionally, we use the four ground-based secondary-eclipse depths published by López-Morales *et al.* (2010) and Croll *et al.* (2011), after correcting for the contri-

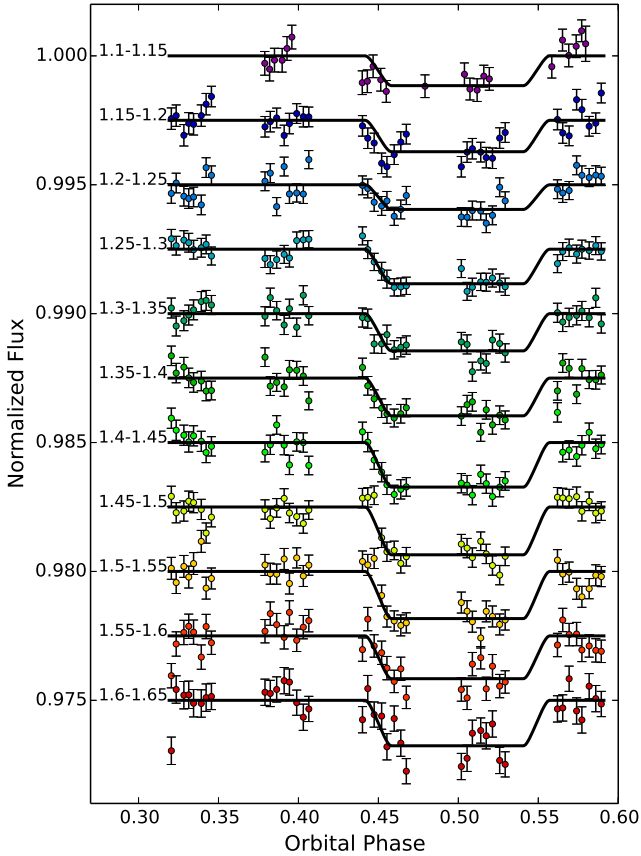


FIG. 4.— WASP-12b spectroscopic light curves from 2011 April 15 using *HST*'s WFC3 instrument. The Divide-White method (Stevenson et al. 2014) produced these results, which are binned, normalized to the system flux, and shifted vertically for ease of comparison. The error bars are 1σ uncertainties and the black lines are best-fit models. The wavelength range for each of the 11 channels is specified in μm . For the bluest channel, we do not model the first orbit or the final batch within each orbit because the flux is systematically higher than the other batches.

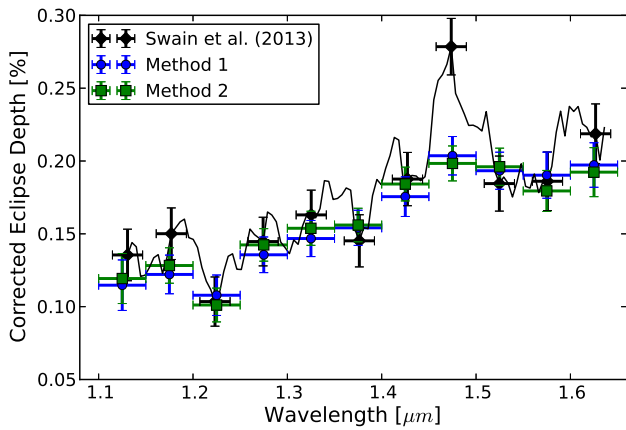


FIG. 5.— WASP-12b corrected emission spectrum using WFC3's G141 grism. Both methods used in our analyses (blue circles and green squares) agree with the results from Swain et al. (2013, black line with diamonds for comparison) in all but one of the spectroscopic channels.

bution from the companion stars. We find corrected depths of $0.085 \pm 0.016\%$, $0.140 \pm 0.030\%$, $0.191 \pm 0.020\%$, and $0.340 \pm 0.014\%$ in the z' , J, H, and K bands, respectively. Despite attempts to include additional photometric measure-

ments by Föhning et al. (2013) and Crossfield et al. (2012), their reported eclipse depths are inconsistent with all of our atmospheric models. Föhning et al. (2013)'s suggestion of variability may be unlikely given the observed consistency in measured *Spitzer* eclipse depths (see Table 2). We recommend that additional observations with longer out-of-eclipse baselines be acquired in these bandpasses to establish more precise and consistent eclipse depths. For completeness, we discuss below how these measurements compare to our derived models.

Using the observed dayside emission spectrum, we apply the atmospheric modeling and retrieval technique described by Madhusudhan (2012) to place constraints on the properties of WASP-12b's atmosphere. We compute model spectra using 1D line-by-line radiative transfer in a plane-parallel atmosphere. This approach assumes local thermodynamic equilibrium, hydrostatic equilibrium, and global energy balance. The models make no assumption about the layer-by-layer radiative equilibrium and, as with the models of Line et al. (2014), impose no constraint on the atmospheric chemical abundances. Thus, our atmospheric retrievals explore both physically plausible and implausible regions of the parameter space.

In this work, we consider three sets of model atmospheres. The first includes line-by-line molecular absorption due to H_2O , CO , CH_4 , and CO_2 ; the second also considers absorption due to C_2H_2 and HCN (see, e.g., Madhusudhan 2012; Moses et al. 2013). Both sets include H_2 - H_2 collision-induced opacities and assign six free parameters for the pressure-temperature profile. TiO and VO do not have features in the wavelength region sampled by these data and are not included. The third set is an isothermal blackbody model that has only one free parameter, the temperature.

When considering only the four primary molecular absorbers, we find a bimodal distribution in the C/O. The C-rich mode ($\text{C/O} \gtrsim 1$) achieves a better fit than the O-rich mode ($\text{C/O} \sim 0.5$, $\Delta\text{BIC} = 9.5$, ~ 120 times more probable); however, both modes require physically implausible atmospheric abundances. Specifically, the best-fit model requires high CH_4 and CO_2 abundances (4.3×10^{-3} and 9.9×10^{-5}), with very little H_2O and CO (4.8×10^{-8} and 9.1×10^{-10} , respectively). However, Madhusudhan (2012) and Moses et al. (2013) demonstrate that the CO_2 abundance in a hot, hydrogen-dominated atmosphere cannot exceed that of H_2O or CO . The solution to this problem lies in the addition of C_2H_2 and HCN to our atmospheric models.

With six molecular absorbers, we explore both O- and C-rich scenarios. For the former, we would expect to detect a broad H_2O absorption feature in the *HST*/WFC3 spectroscopic data. This is not the case, so the O-rich models must adopt a predominantly isothermal profile at pressures $\gtrsim 0.01$ bar (which are the depths probed by WFC3) and decrease the H_2O abundance by a factor of five relative to solar composition. Furthermore, C_2H_2 and HCN are not thermochemically favored in an O-rich atmosphere; therefore, to fit the shallow eclipse depth at $4.5 \mu\text{m}$, the models compensate by increasing the CO_2 abundance by two orders of magnitude relative to solar composition. As a result, the best-fit O-rich model ($\chi^2 \sim 50$) remains physically implausible with its strong CO_2 feature at $4.5 \mu\text{m}$ and insignificant H_2O absorption. The lack of H_2O absorption in the WFC3 bandpass and the low $4.5 \mu\text{m}$ photometry point are more readily explained by C-rich models ($\chi^2 \sim 38$). These models naturally explain the lack of H_2O due to insufficient oxygen after the formation of CO , and they

TABLE 4
ATMOSPHERIC MODEL COMPARISON

Model Type	χ^2_{Phot}	χ^2_{Spec}	χ^2_{Total}	ΔBIC
Carbon-rich	17.2	20.4	37.6	0.0
Oxygen-rich	31.0	19.6	50.6	13.0
Blackbody	79.9	19.1	99.0	31.6

TABLE 5
BEST-FIT MOLECULAR ABUNDANCES

Model	H ₂ O ^a	CO	CH ₄
Oxygen-rich	5.0×10^{-4}	5.0×10^{-4}	1.0×10^{-7}
Carbon-rich	2.3×10^{-7}	3.4×10^{-4}	8.3×10^{-5}
	CO ₂	C ₂ H ₂	HCN
Oxygen-rich	6.7×10^{-5}	1.6×10^{-10}	1.0×10^{-7}
Carbon-rich	9.0×10^{-7}	1.0×10^{-5}	1.0×10^{-6}

^aThe H₂O abundance in the C-rich model has very little impact on the observed spectrum at these low levels and can easily be a factor of four larger, thus maintaining physical plausibility.

utilize C₂H₂ and HCN (in addition to CO₂) to explain the absorption at 4.5 μm .

Although the WFC3 measurements are consistent with an isothermal blackbody model, the broadband *Spitzer* points preclude such an option. The 4.5 μm eclipse depth, which we derived from four independent datasets with consistent results, is discrepant from the isothermal model at a significance of 7σ .

In Table 4, we compare our best-fit models from the six-molecule and isothermal-blackbody scenarios to the photometric and spectroscopic data. Table 4 also presents differences in BIC values. BIC is similar to χ^2 , but it adds a penalty for using additional free parameters; therefore, smaller BIC values are preferable (Liddle 2007). Using this information, we conclude that the C-rich model is 670 times more probable than the O-rich model and 7.3×10^6 times more probable than a blackbody.

Table 5 lists the derived molecular abundances for the best-fit, six-molecule O- and C-rich models; their carbon-to-oxygen ratios are 0.5 and 1.2, respectively. We compare these results to the best-fit ellipsoidal solution presented by Line *et al.* (2014, {H₂O, CO, CH₄, CO₂} = { 5.12×10^{-4} , 2.17×10^{-3} , 2×10^{-10} , 1.07×10^{-1} }), which uses a 4.5 μm eclipse depth that is consistent with our own result. Other spectroscopic and photometric data points from their ellipsoidal solution are also generally consistent with, but not necessarily identical to, our own measurements. For example, our eclipse depths at 3.6 and 4.5 μm are 4.0 and 2.8 times more precise. We find that our best-fit C-rich model favors $6.4 \times$ less CO, $\sim 415,000 \times$ more CH₄, and $\sim 63,000 \times$ less CO₂. The latter two molecular abundances are outside of the 68% confidence intervals published by Line *et al.* (2014). Their lack of CH₄ can be explained by their preferred low C/O; however, their 10% CO₂ abundance is irreproducible, even when compared to our four-molecule fits, whose implausibly large CO₂ abundances do not exceed 1×10^{-4} .

Madhusudhan (2012) and Moses *et al.* (2013) demonstrate that in an O-rich, hydrogen-dominated atmosphere, the concentration of CH₄, CO, or CO₂ cannot exceed that of H₂O, regardless of its state of chemical equilibrium. Line *et al.* (2014) list CO and CO₂ abundance ratios in their WASP-12b best-fit solutions that far exceed that of H₂O. Madhusudhan

(2012) and Moses *et al.* (2013) also determine that the CO abundance in a hot, hydrogen-dominated atmosphere must exceed that of CH₄ and CO₂. Again, Line *et al.* (2014) report a best-fit CO₂ value that is inconsistent with this theory. Finally, Line *et al.* (2014) do not include C₂H₂ or HCN in their abundance retrieval analysis. Both molecules are expected to be prevalent in a C-rich atmosphere and both have features in *Spitzer*'s 4.5 μm bandpass. Without these molecules, Line *et al.* (2014) rely on an unrealistically-large CO₂ abundance to explain the relatively shallow eclipse depth at 4.5 μm .

In Figure 6, we present the corrected dayside emission spectrum of WASP-12b and the best-fit atmospheric models (which include C₂H₂ and HCN). For reference, we also add the z' secondary-eclipse measurement from Föhring *et al.* (2013) and the narrow-band 2.315- μm measurement from Crossfield *et al.* (2012). Although none of the atmospheric models provides a reasonable fit to these additional data points, the depth measured by Föhring *et al.* (2013) further decreases the prospect of an O-rich atmosphere, while the depth reported by Crossfield *et al.* (2012) relies on fitting short baselines before and after secondary eclipse. There have been numerous ground-based broadband photometry measurements of transiting exoplanets with reported depths in excess of model predictions (e.g., Rogers *et al.* 2009; Gillon *et al.* 2009; Gibson *et al.* 2010; Croll *et al.* 2011). Rogers *et al.* (2013) suggest that, in the event of red noise, these measurements may be biased in one direction or another, thus making ground-based photometry measurements less reliable than previously thought.

In Figure 7, we present the thermal profiles and flux contribution functions for the O- and C-rich models from Figure 6. In contrast to profiles presented by Line *et al.* (2014), neither scenario favors a thermal inversion. Our best-fit C-rich thermal profile is constant at pressure levels $\gtrsim 0.1$ bar, which is in good agreement with the results presented by Line *et al.* (2014); however, the profiles diverge as our temperature decreases monotonically with decreasing pressure and their temperature increases, thus indicating an inversion.

Sing *et al.* (2013) and Stevenson *et al.* (2014) both present evidence for clouds or hazes in the atmosphere of WASP-12b at its terminator. However, light paths through the atmosphere are much shorter ($\sim 40 \times$) with emission spectroscopy than they are with transmission spectroscopy, given the latter's slant optical path length (Fortney 2005). Therefore, the presence of clouds or hazes should have a smaller cumulative effect on the observed emission spectrum. The detection of spectral features in the dayside emission spectrum rules out the presence of a fully opaque, high-altitude dayside cloud layer. If a thick cloud layer does exist on the dayside, it must be at pressure levels $\gtrsim 0.1$ bar, where the thermal profile is isothermal.

5. CONCLUSIONS

Through our uniform reanalysis of all available WASP-12b secondary-eclipse data from both *HST* and *Spitzer*, we have provided a consistent dataset from which to draw atmospheric conclusions. This is particularly important for the three 3.6 μm and four 4.5 μm *Spitzer* observations, which no longer exhibit discrepant eclipse depths. This new analysis also uniformly corrected the measured eclipse depths due to contamination from the binary companion WASP-12BC.

To explain WASP-12b's observed dayside emission spectrum, we examined three sets of model atmospheres (four

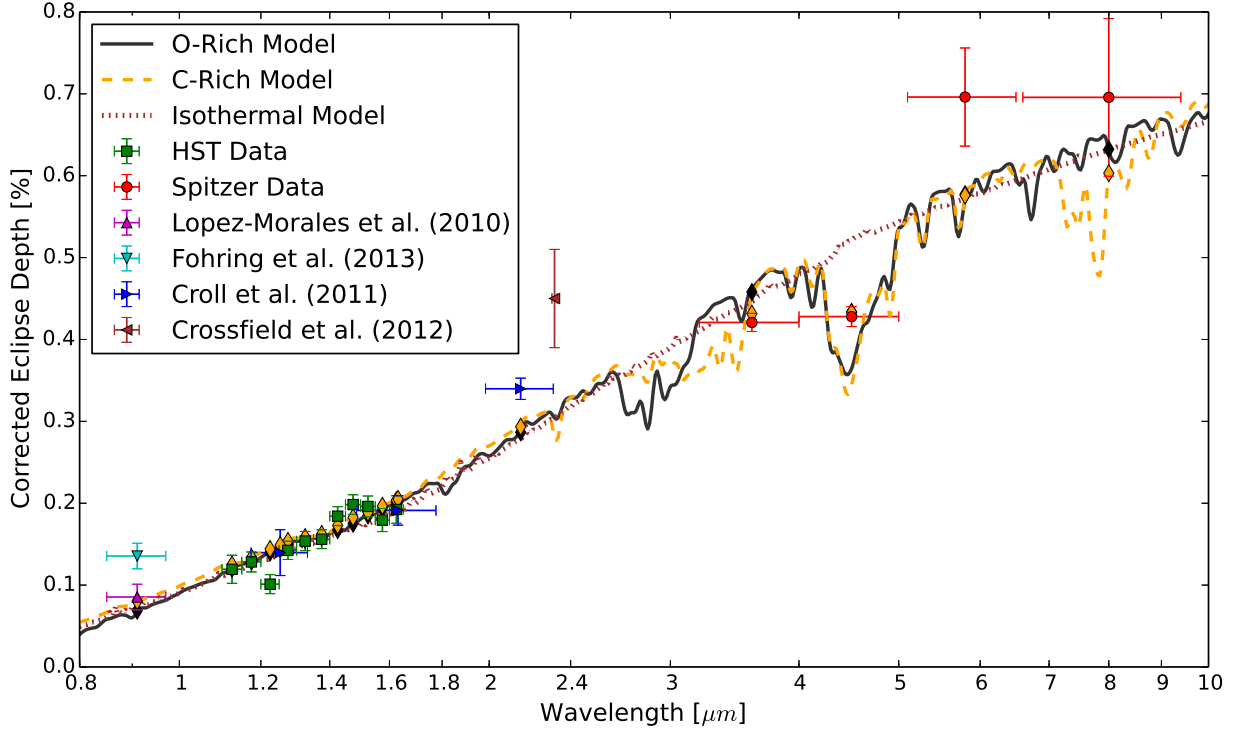


FIG. 6.— WASP-12b corrected dayside emission spectrum with atmospheric models. We fit oxygen-rich, carbon-rich, and isothermal blackbody atmospheric models (solid black, dashed orange, and dotted brown lines, respectively) to the *HST*/WFC3 points (green squares) in the NIR, the *Spitzer*/IRAC points (red circles) from 3 – 10 μm , and the ground-based points from López-Morales et al. (2010) and Croll et al. (2011). For reference, we also plot the z' and 2.315- μm measurements from Föhrling et al. (2013) and Crossfield et al. (2012), respectively. The isothermal model has a blackbody temperature of 2930 K. The best-fit oxygen-rich model requires $5\times$ less H_2O and $\sim 100\times$ more CO_2 than solar composition. This physically-implausible scenario achieves a better fit than all oxygen-rich, solar-composition models. However, in comparing the bandpass-integrated models (colored diamonds) to the available data, the carbon-rich model achieves the best fit by a ΔBIC of 13.0 (670 times more probable than the best O-rich model).

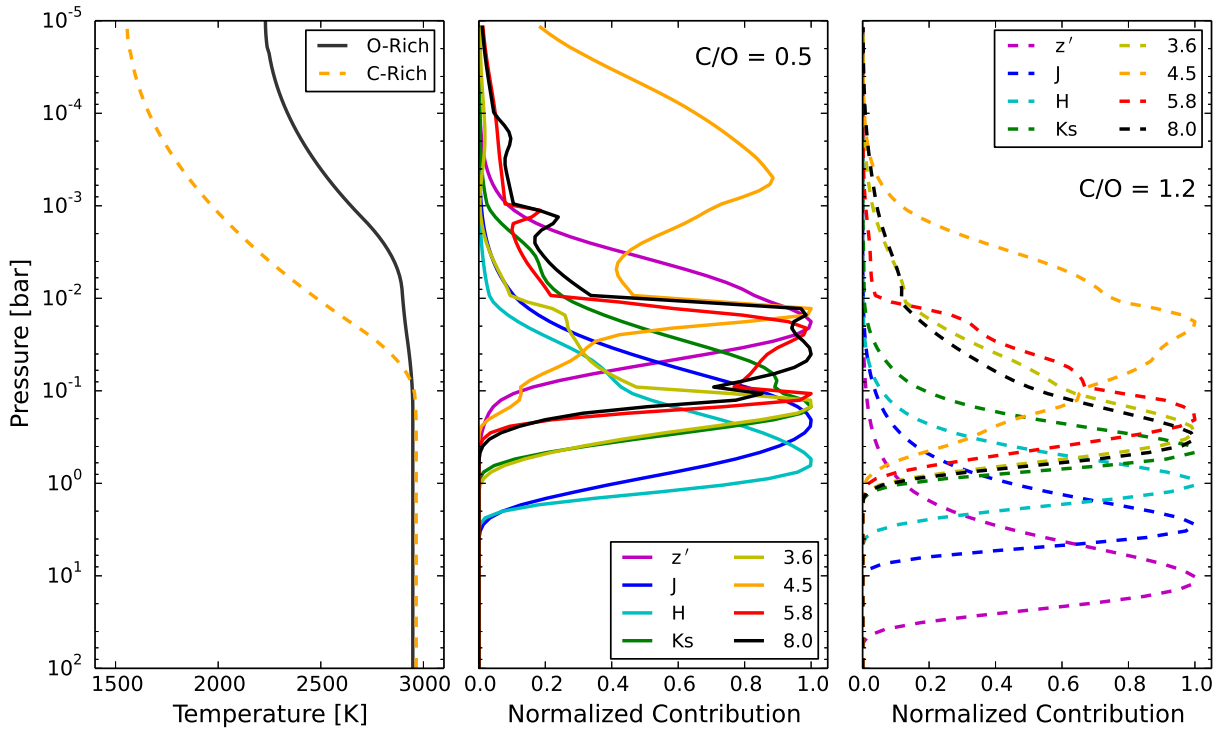


FIG. 7.— WASP-12b pressure-temperature profiles and contribution functions. The left panel shows that the O-rich (solid line) and C-rich (dashed line) models have monotonically decreasing temperature profiles with decreasing pressure. The center and right panels illustrate the atmospheric flux origin observed in each photometric bandpass for the O-rich and C-rich models, respectively. The majority of *HST*/WFC3's contribution (not shown) resides in the nearly-isothermal region deeper than 0.01 bar.

molecules, six molecules, and an isothermal blackbody). All models that consider molecular absorption due to only H₂O, CO, CH₄, and CO₂ require physically implausible atmospheric abundances. Nonetheless, these models find that a C-rich scenario is ~ 120 times more probable ($\Delta\text{BIC} = 9.5$) than an O-rich scenario. With the addition of C₂H₂ and HCN, the C-rich models find physically plausible solutions and continue to achieve the best fits. The combination of photometric and spectroscopic data rule out the best-fit six-molecule O-rich and isothermal models at a high statistical significance ($\Delta\text{BIC} = 13.0$ and 31.6 , respectively). A non-isothermal emission spectrum can be confirmed visually in Figure 6, where the isothermal model is rejected at $4.5\ \mu\text{m}$ with a significance of 7σ . We conclude that, when we account for opacity due to C₂H₂ and HCN, a dayside atmosphere with a $\text{C/O} \geq 1$ is the most plausible scenario. We also emphasize that the inclusion of chemical limits in the Bayesian phase-space exploration has a major effect on the composition retrieval. These results reaffirm that the C/O is an important facet to consider in exoplanet characterization that may provide clues to likely planet formation and migration scenarios.

Forthcoming WFC3 data will provide a high-precision correction to WASP-12's stellar companion and will place tighter

constraints on the planet's transmission spectrum. Thus, we leave for future work the application of a temperature and abundance retrieval method to both the transmission and emission spectra. Such work will attempt to assemble a more consistent description of WASP-12b's composition, thermal profile, and C/O between its dayside and terminator regions.

We thank contributors to SciPy, Matplotlib, and the Python Programming Language, the free and open-source community, the NASA Astrophysics Data System, and the JPL Solar System Dynamics group for software and services. This research made use of Tiny Tim/Spitzer, developed by John Krist for the Spitzer Science Center. The Center is managed by the California Institute of Technology under a contract with NASA. Funding for this work has been provided by NASA grants NNX13AF38G and NNX13AJ16G. J.L.B. acknowledges support from the Alfred P. Sloan Foundation. N.M. acknowledges support from the Yale Center for Astronomy and Astrophysics (YCAA) at Yale University through the YCAA prize fellowship.

REFERENCES

- Agol, E., Cowan, N. B., Knutson, H. A., et al. 2010, *ApJ*, 721, 1861
 Barman, T. S., Hauschildt, P. H., & Allard, F. 2001, *ApJ*, 556, 885
 —. 2005, *ApJ*, 632, 1132
 Bechter, E. B., Crepp, J. R., Ngo, H., et al. 2014, *ApJ*, 788, 2
 Bergfors, C., Brandner, W., Daemgen, S., et al. 2013, *MNRAS*, 428, 182
 Berta, Z. K., Charbonneau, D., Désert, J.-M., et al. 2012, *ApJ*, 747, 35
 Campo, C. J., Harrington, J., Hardy, R. A., Stevenson, K. B., et al. 2011, *ApJ*, 727, 125
 Charbonneau, D., et al. 2005, *ApJ*, 626, 523
 Cowan, N. B., Machalek, P., Croll, B., et al. 2012, *ApJ*, 747, 82
 Croll, B., Lafreniere, D., Albert, L., et al. 2011, *AJ*, 141, 30
 Crossfield, I. J. M., Barman, T., Hansen, B. M. S., Tanaka, I., & Kodama, T. 2012, *ApJ*, 760, 140
 Cubillos, P., Harrington, J., Madhusudhan, N., et al. 2013, *ApJ*, 768, 42
 Deming, D., Wilkins, A., McCullough, P., et al. 2013, *ApJ*, 774, 95
 Fazio, G. G., et al. 2004, *Astrophys. J. Suppl. Ser.*, 154, 10
 Föhring, D., Dhillon, V. S., Madhusudhan, N., et al. 2013, *MNRAS*, 435, 2268
 Fortney, J. J. 2005, *MNRAS*, 364, 649
 Gibson, N. P., Aigrain, S., Pollacco, D. L., et al. 2010, *MNRAS*, 404, L114
 Gillon, M., Demory, B.-O., Triaud, A. H. M. J., et al. 2009, *A&A*, 506, 359
 Harrington, J., Luszcz, S., Seager, S., Deming, D., & Richardson, L. J. 2007, *Nature*, 447, 691
 Hebb, L., Collier-Cameron, A., Loeillet, B., et al. 2009, *ApJ*, 693, 1920
 Knutson, H. A., et al. 2011, *ApJ*, 735, 27
 Kreidberg, L., Bean, J. L., Désert, J.-M., et al. 2014, *Nature*, 505, 69
 Lewis, N. K., Knutson, H. A., Showman, A. P., et al. 2013, *ApJ*, 766, 95
 Liddle, A. R. 2007, *Mon. Not. R. Astron. Soc.*, 377, L74
 Line, M. R., Knutson, H., Wolf, A. S., & Yung, Y. L. 2014, *ApJ*, 783, 70
 López-Morales, M., Coughlin, J. L., Sing, D. K., et al. 2010, *ApJ*, 716, L36
 Madhusudhan, N. 2012, *ApJ*, 758, 36
 Madhusudhan, N., Harrington, J., Stevenson, K. B., et al. 2011, *Nature*, 469, 64
 Mandel, K., & Agol, E. 2002, *ApJ*, 580, L171
 Moses, J. I., Madhusudhan, N., Visscher, C., & Freedman, R. S. 2013, *ApJ*, 763, 25
 Pont, F., Zucker, S., & Queloz, D. 2006, *MNRAS*, 373, 231
 Rogers, J., López-Morales, M., Apai, D., & Adams, E. 2013, *ApJ*, 767, 64
 Rogers, J. C., Apai, D., López-Morales, M., Sing, D. K., & Burrows, A. 2009, *ApJ*, 707, 1707
 Sing, D. K., Lecavelier des Etangs, A., Fortney, J. J., et al. 2013, *MNRAS*, 436, 2956
 Stevenson, K. B., Bean, J. L., Seifahrt, A., et al. 2014, *AJ*, 147, 161
 Stevenson, K. B., Harrington, J., Fortney, J. J., Lored, T. J., et al. 2012, *ApJ*, 754, 136
 Swain, M., Deroo, P., Tinetti, G., et al. 2013, *Icarus*, 225, 432
 Todorov, K., Deming, D., Harrington, J., et al. 2010, *ApJ*, 708, 498
 Winn, J. N., Holman, M. J., Torres, G., et al. 2008, *ApJ*, 683, 1076